# Synergistic effect between anatase and rutile $TiO_2$ nanoparticles in dye-sensitized solar cells†

**Gonghu Li, Christiaan P. Richter, Rebecca L. Milot, Lawrence Cai, Charles A. Schmuttenmaer,* Robert H. Crabtree,* Gary W. Brudvig* and Victor S. Batista***

***Received 1st May 2009, Accepted 17th August 2009***
***First published as an Advance Article on the web 2nd September 2009***
**DOI: 10.1039/b908686b**



A synergistic effect between anatase and rutile $TiO_2$ is known, in which the addition of rutile can remarkably enhance the photocatalytic activity of anatase in the degradation of organic contaminants. In this study, mixed-phase $TiO_2$ nanocomposites consisting of anatase and rutile nanoparticles (NPs) were prepared for use as photoanodes in dye-sensitized solar cells (DSSCs) and were characterized by using UV-vis spectroscopy, powder X-ray diffraction and scanning electron microscopy. The addition of 10–15% rutile significantly improved light harvesting and the overall solar conversion efficiency of anatase NPs in DSSCs. The underlying mechanism for the synergistic effect in DSSCs is now explored by using time-resolved terahertz spectroscopy. It is clearly demonstrated that photo-excited electrons injected into the rutile NPs can migrate to the conduction band of anatase NPs, enhancing the photocurrent and efficiency. Interfacial electron transfer from rutile to anatase, similar to that in heterogeneous photocatalysis, is proposed to account for the synergistic effect in DSSCs. Our results further suggest that the synergistic effect can be used to explain the beneficial effect of $TiCl_4$ treatment on DSSC efficiency.

## Introduction

Dye-sensitized solar cells (DSSCs) have emerged as promising alternatives for expensive solid-state photovoltaic devices since the seminal work by O'Regan and Grätzel in 1991.[1] A DSSC consists of a dye molecule, semiconducting photoanode, redox mediator, and counter electrode; its operating principle is well understood.[2–5] The photoanode, typically a mesoscopic $TiO_2$ thin film, is placed in contact with an electrolyte containing the $I_3^-/I^-$ redox couple. Following light absorption and photoexcitation of the dye molecule, an electron is rapidly injected into the conduction band of $TiO_2$ nanoparticles (NPs). The injected electron then diffuses through the $TiO_2$ NP network to be collected and passed through the external load. The oxidized dye molecule is regenerated by electron donation from the electrolyte. The oxidized electrolyte is in turn regenerated at the counter electrode by electrons passed through the external load. Undesired processes competing with the interfacial electron transfer (IET) from the dye to the $TiO_2$ conduction band include: decay of the excited dye molecule before it injects an electron, recombination of the injected electron with the oxidized dye before the dye is regenerated, and interception of an electron from the photoanode by the redox mediator before it is collected.[6]

Understanding the photochemical and photophysical properties of dye-sensitized $TiO_2$ NPs has enabled the molecular control of IET and the optimization of solar energy conversion using DSSCs.[7–9] Currently, the maximum solar conversion efficiency using a DSSC is approximately 11.2%.[10] Recent research efforts have been directed toward further improving the efficiency by optimizing the dye, redox mediator, and/or photoanode.[6] For example, the dye structures can be tuned to improve the molar extinction coefficient and solar light harvesting capacity, thereby increasing the photocurrent and efficiency.[11–13] New architectures for the photoanode, including different $TiO_2$ nanostructures such as nanotubes and nanowires, have been designed to enhance the photovoltaic performance of DSSCs.[14–16] In addition, the mesoporosity of the $TiO_2$ thin film[17] and the crystal orientation of $TiO_2$ NPs[18–20] have been found to affect dye adsorption and IET.

The crystal structure of $TiO_2$ also plays a factor in designing the most efficient DSSCs. Anatase is the preferred crystal polymorph for use in DSSCs partly due to the difference in the flat-band potential of anatase and rutile. Because the anatase conduction band is 0.2 V more negative than that of rutile, a larger maximum photovoltage can be obtained on anatase than on rutile if the same redox mediator is employed.[21,22] Kambe and co-workers showed that the diffusion coefficient of conduction band electrons in rutile is significantly smaller than that in anatase.[23] The researchers initiated band-gap excitation with a UV laser, which led to the formation of conduction band electrons and valence band holes.[23] Subsequently, time-resolved photocurrent measurements were carried out in the presence of ethanol as a hole scavenger, which inhibits electron-hole recombination and enables the measurement of electron diffusion coefficients.[23] However, Park and co-workers found that the photocurrent-voltage responses of dye-sensitized rutile and anatase films were remarkably close.[24] In their study, the open-circuit voltage was essentially the same for the two films, whereas the short-circuit photocurrent of the rutile film was only

*Department of Chemistry, Yale University, P. O. Box 208107, New Haven, CT 06520-8107. E-mail: charles.schmuttenmaer@yale.edu, robert.crabtree@yale.edu, gary.brudvig@yale.edu, victor.batista@yale.edu*

† Electronic supplementary information (ESI) available: Fig. S1: Normalized 400 nm pump/THz probe of electron injection in N719-sensitized $TiO_2$ films: (a) R0, (b) R5, (c) R13, (d) R19, (e) R40, and (f) R100. See DOI: 10.1039/b908686b

 

about 30% lower than that of the anatase film.[24] The researchers attributed the lower photocurrent of the rutile film to a lesser amount of adsorbed dye due to a smaller surface area per unit volume compared with that of the anatase film.[24]

As heterogeneous photocatalysts for environmental applications, anatase is the preferred polymorph because anatase usually demonstrates higher activity than rutile.[25,26] In photocatalysis, efficiencies are largely limited by detrimental electron-hole recombination. A greater extent of charge recombination in rutile is considered responsible for the generally lower photocatalytic activity of rutile in comparison to anatase.[25,26] An interesting synergistic effect exists between anatase and rutile in mixed-phase $TiO_2$ nanocomposites as photocatalysts.[27–35] Specifically, the addition of relatively inactive rutile significantly enhances the photocatalytic activity of anatase.[27,28] The commercially available Degussa P25, the gold standard for photocatalysts because of its superior activity, is indeed a mixed-phase $TiO_2$ material consisting of 85% anatase and 15% rutile.[36] Gray, Rajh, and co-workers studied the photochemistry of mixed-phase $TiO_2$ nanocomposites using electron paramagnetic resonance (EPR) spectroscopy.[27,28] They discovered that interfacial charge separation between anatase and rutile NPs contributes to the improved photocatalytic activities of mixed-phase $TiO_2$ nanocomposites.[27,28] With anatase and rutile in close contact, photo-excited electrons and holes were preferentially trapped in the anatase and rutile phases, inhibiting the detrimental electron-hole recombination.[25]

A similar synergistic effect exists between anatase and rutile when mixed-phase $TiO_2$ nanocomposites are used in DSSCs. Koo and co-workers synthesized $TiO_2$ nanorods with varying particle sizes and crystal phases.[37] The researchers found that the mixed-phase $TiO_2$ demonstrated higher solar conversion efficiency than pure-phase anatase or rutile in DSSCs.[37] Contradictory results have been reported in the literature, in which pure anatase showed higher efficiency as the photoanode than mixed-phase $TiO_2$.[38,39] In these studies, the crystal phase was varied together with other parameters including the particle size, morphology, and mesoporosity of $TiO_2$ materials. Because these parameters could potentially influence dye adsorption and IET, a conclusive comparison between pure- and mixed-phase $TiO_2$ materials as DSSC photoanodes cannot be obtained based on these studies. Furthermore, a mechanistic explanation for the different performance of mixed-phase $TiO_2$ *vs.* pure-phase materials in DSSCs remains elusive.

Here, anatase and rutile NPs are used to prepare a series of mixed-phase $TiO_2$ nanocomposites. Photoanodes are then prepared from the mixed-phase nanocomposites and are tested in DSSCs. Because the photoanodes differ only in phase composition, this study clearly confirms the influence of $TiO_2$ phase composition on the overall solar conversion efficiency of DSSCs. Electron paramagnetic resonance spectroscopy was widely applied in studying $TiO_2$ photochemistry partly because of its ability to probe trapped electrons in the form of paramagnetic $Ti^{3+}$ species. However, electrons in the $TiO_2$ conduction band are EPR-silent.[40] Time-resolved terahertz (THz) spectroscopy has emerged as a powerful technique to follow the IET from surface coordination compounds to the $TiO_2$ conduction band.[41] In this study, the IET in dye-sensitized mixed-phase $TiO_2$ is studied with THz spectroscopy in order to better understand the synergistic interactions between anatase and rutile in DSSCs.

## Results and discussion

### Characterization of $TiO_2$ nanocomposites

It is well known that rutile is the favored polymorph under acidic conditions in hydrothermal synthesis.[42,43] In this study, pure-phase rutile NPs were synthesized *via* a low-temperature hydrothermal method using $TiCl_4$ as the Ti precursor.[44] The hydrolysis of $TiCl_4$ led to the formation of hydrochloric acid in addition to a $TiO_2$ sol, which was then refluxed to facilitate the formation of pure-phase rutile. A commercially available anatase sample was mixed with different amounts of rutile in order to prepare mixed-phase $TiO_2$ nanocomposites with varying phase composition. Powder X-ray diffraction (XRD) was used to determine the phase composition of $TiO_2$ materials.

Fig. 1 shows the anatase and rutile diffraction patterns of different $TiO_2$ materials after thermal treatment at 450 °C. In this study, the commercial anatase and the synthesized rutile are denoted R0 and R100, respectively, with the numbers representing the rutile content. As can be inferred from Fig. 1a, the anatase NPs are well-crystallized as indicated by the sharp diffraction from anatase (101) planes. Only the diffraction pattern associated with rutile crystal faces is seen in Fig. 1f, confirming that pure-phase rutile was synthesized by the hydrothermal method. The broad diffraction from the rutile (110) face implies a relatively low degree of crystallinity of the synthesized rutile $TiO_2$.

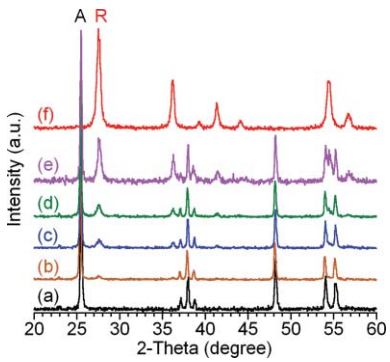


**Fig. 1** XRD patterns of $TiO_2$ materials: (a) R0, (b) R5, (c) R13, (d) R19, (e) R40, and (f) R100. The diffractions of anatase (101) and rutile (110) are labelled in the figure as "A" and "R", respectively. Traces (a)–(e) are normalized such that the anatase (101) peaks have the same intensity.

The phase composition of $TiO_2$ nanocomposites can be determined from XRD results according to eqn (1):

$$W_R = \frac{A_R}{0.884 \times A_A + A_R} \quad (1)$$

where $W_R$, $A_A$, and $A_R$ represent the rutile weight percentage, integrated intensity of anatase (101) peak, and integrated intensity of rutile (110) peak, respectively.[45] As can be seen from Fig. 1(b–e), $TiO_2$ nanocomposites with different amounts of rutile were obtained. The weight percentages of rutile in the four mixed-phase nanocomposites were determined to be 4.5, 12.8, 18.8, and 40.2 wt%. In this study, these mixed-phase $TiO_2$ materials are denoted R5, R13, R19, and R40, respectively.

Thin films of synthesized $TiO_2$ nanocomposites were also prepared as photoanodes on fluoride-doped tin oxide (FTO) conducting glasses. Thermal treatment at 450 °C was applied

to the photoanodes to ensure good electrical contact between $TiO_2$ NPs with the FTO layer. Prior to dye-sensitization for use in DSSCs, the photoanodes were examined with scanning electron microscopy (SEM). Fig. 2 shows representative SEM images of different photoanodes. The photoanode prepared from the commercial anatase consists of nearly spherical $TiO_2$ NPs having an average particle size around 100 nm (R0, Fig. 2a).[33] It can be seen from Fig. 2 that the synthesized rutile NPs are nanorods with dimensions of ~20 nm in diameter and ~100 nm in length. The anatase NPs and rutile nanorods are well mixed on the photoanodes prepared from mixed-phase $TiO_2$ materials (Fig. 2b–d). At relatively high rutile content, the rutile nanorods formed aggregates, as can be seen from the SEM images of R40 and R100 (Fig. 2e and f).

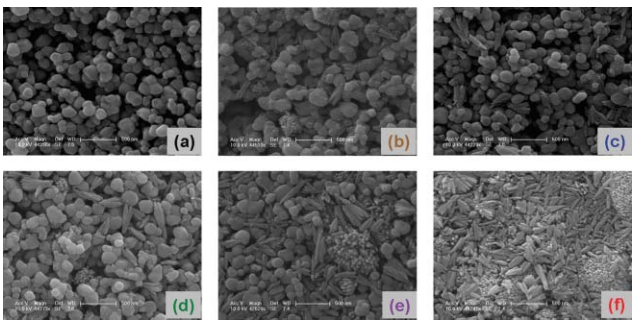


**Fig. 2** SEM images of $TiO_2$ photoanodes prepared from: (a) R0, (b) R5, (c) R13, (d) R19, (e) R40, and (f) R100. The photoanodes were sintered at 450 °C for 2 h. Scale bars are 500 nm.

Pure $TiO_2$ materials barely absorb visible light with wavelengths greater than 400 nm. In DSSCs, $TiO_2$ NPs are sensitized with dye molecules to harvest the natural sunlight. The most studied and most efficient devices to date use a ruthenium-based dye, $RuL_2(NCS)_2{\cdot}2TBA$, where L = 2,2′-bipyridyl-4,4′-dicarboxylic acid and TBA = tetrabutylammonium, which is referred to as N719.[46] In this study, the N719 dye was chosen to sensitize the thin films of different $TiO_2$ materials. The UV-vis spectra shown in Fig. 3 indicate that the absorption edges of synthesized $TiO_2$ materials were successfully extended to the visible region. In contrast with pure-phase anatase (R0, Fig. 3a), mixed-phase $TiO_2$ nanocomposites after N719-sensitization absorb a much greater portion of the visible light (Fig. 3b–e), indicating the addition of rutile nanorods significantly enhanced the dye loading. Generally,

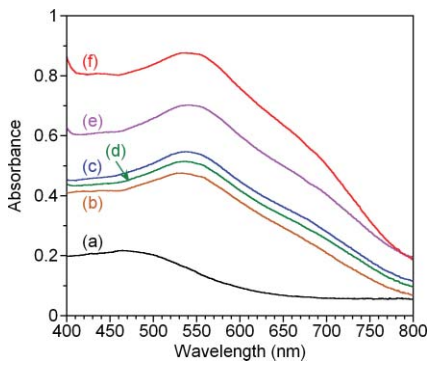


**Fig. 3** UV-vis spectra of N719-sensitized $TiO_2$ films: (a) R0, (b) R5, (c) R13, (d) R19, (e) R40, and (f) R100.

the sensitized $TiO_2$ materials containing more rutile have greater absorbance in the visible light region. The specific surface areas of R0, R5, R13, R19, R40, and R100 were measured to be 9.9, 10.2, 12.3, 15.8, 14.5, and 24.5 $m^2\ g^{-1}$, respectively. Thus, surface area differences partly account for the difference shown in Fig. 3.

### Solar cell performance

In this study, $TiO_2$ photoanodes were sensitized with N719 and assembled into DSSCs. Photocurrent–voltage ($I$–$V$) measurements were carried out using a digital source meter under an applied external potential scan. Fig. 4 shows the $I$–$V$ curves of three DSSCs in the dark and under simulated solar light with an intensity of 100 mW $cm^{-2}$. Among the three cells, the P25 cell produced the highest photocurrent, while the rutile cell generated higher photocurrent in comparison to the anatase cell. Because the surface areas of P25, rutile nanorods, and anatase NPs were measured to be 50,[47] 24.5, and 9.9 $m^2\ g^{-1}$, respectively, the difference in photocurrent is largely attributed to the differences in the surface area and dye loading. The open-circuit photovoltage of the P25 cell is slightly lower that those of rutile and anatase, and the dark current of the P25 cell is the highest among the three cells. This is likely due to the relatively higher surface area of P25 NPs and subsequently a greater degree of electron interception by $I_3^-$ in the P25 cell.

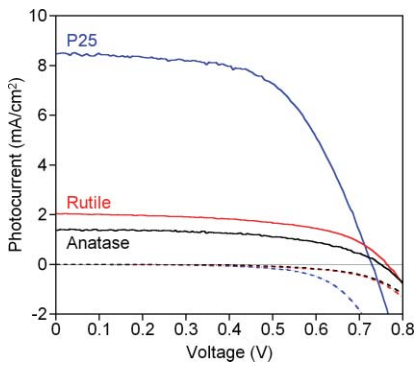


**Fig. 4** Photocurrent density–voltage curves of DSSCs using N719-sensitized photoanodes prepared from Degussa P25, rutile (R100), and anatase (R0) NPs. Light intensity was 100 mW $cm^{-2}$. The $I$–$V$ curves in dark (dashed lines) are also plotted in the figure.

In a DSSC, the overall solar conversion efficiency ($\eta$) is a product of the short-circuit current density ($I_{SC}$), the open-circuit photovoltage ($V_{OC}$), and the fill factor ($FF$), according to:

$$\eta = \frac{I_{SC} \times V_{OC} \times FF}{P_{in}} \quad (2)$$

where $P_{in}$ is the total light incident on the cell (100 mW $cm^{-2}$).[6] For each cell, $I_{SC}$ and $V_{OC}$ can be derived directly from its $I$–$V$ curve such as those shown in Fig. 4. The fill factor is the ratio of the maximum cell power to the product of $I_{SC}$ and $V_{OC}$. The overall efficiency was calculated according to eqn (2). Table 1 lists the $I$–$V$ parameters of DSSCs prepared from different $TiO_2$ materials.

It can be seen from Table 1 that the highest overall efficiency (3.64%) was obtained from the P25 cell. The anatase (R0) cell gave an efficiency of 0.57%, in contrast with 0.87% for the rutile (R100) cell. Significantly higher efficiencies were obtained from

 

**Table 1** *I–V* parameters of DSSCs under simulated sunlight (light intensity 100 mW cm$^{-2}$).[a]

| Photoanode | $V_{OC}$/V | $I_{SC}$/mA cm$^{-2}$ | *FF* | $\eta$ (%) |
|---|---|---|---|---|
| R0 | 0.75 (0.72) | 1.37 (2.74) | 0.55 (0.56) | 0.57 (1.11) |
| R5 | 0.78 (0.76) | 4.31 (6.66) | 0.57 (0.48) | 1.91 (2.45) |
| R13 | 0.71 (0.70) | 5.84 (7.96) | 0.51 (0.49) | 2.11 (2.72) |
| R19 | 0.70 (0.67) | 5.26 (7.42) | 0.49 (0.47) | 1.81 (2.34) |
| R40 | 0.66 (0.61) | 4.00 (6.25) | 0.46 (0.46) | 1.21 (1.75) |
| R100 | 0.76 (0.70) | 2.05 (4.08) | 0.56 (0.51) | 0.87 (1.47) |
| P25 | 0.73 (0.72) | 8.47 (13.23) | 0.59 (0.48) | 3.64 (4.59) |

[a] *I–V* parameters of DSSCs with $TiCl_4$ treatment are listed in parentheses.

DSSCs using mixed-phase $TiO_2$ nanocomposites than the anatase or rutile cell (Table 1). At relatively low rutile content, the cell performance was enhanced by the addition of rutile because the efficiencies follow this trend: R13 > R5 > R0. Further addition of rutile to the mixed-phase $TiO_2$ appeared to be detrimental to the cell efficiencies (R13 > R19 > R40 > R100). The comparison highlights the existence of a synergistic effect between the anatase and rutile phases in DSSCs. The strongest synergistic effect between the anatase and rutile phases occurs in the R13 cell, suggesting an optimal rutile percentage around 13 wt% for the best performance using mixed-phase DSSCs.

The comparison of photocurrent is similar to that of efficiency because the differences in the open-circuit photovoltage and the fill factor are much less significant. The R13 cell gave both the highest efficiency (2.11%) and photocurrent (5.84 mA cm$^{-2}$) among the mixed-phase DSSCs. A higher photocurrent was obtained from the R19 cell than the R5 cell although the latter gave a better efficiency than the former. This discrepancy can be explained by the observation that the open-circuit photovoltage (and the fill factor) decreases as the rutile content increases in mixed-phase DSSCs, as shown in Table 1. In other words, a relatively greater open-circuit photovoltage (and fill factor) from the R5 cell compensated its lower photocurrent in contrast with the R19 cell.

### Time-resolved THz investigation

Time-resolved THz spectroscopy is employed to investigate the underlying mechanism responsible for the synergistic effect between anatase and rutile in DSSCs. Because THz radiation is absorbed by free electrons in the conduction band of $TiO_2$ NPs, the time scale and efficiency of charge injection into $TiO_2$ NPs can be compared with sub-picosecond temporal resolution.[48] Moreover, the magnitude of the decrease in THz transmission scales directly with the concentration of free carriers multiplied by their mobility. In dye-sensitized $TiO_2$ NPs, photoexcitation and subsequent electron injection causes the free carrier population in the $TiO_2$ to increase. Thus, electron injection from N719 to the $TiO_2$ conduction band leads to decay in the THz transmission amplitude that scales with the product of the number and mobility of the injected carriers.

In this study, the same dye-sensitized $TiO_2$ thin films were used in both UV-vis measurements and THz studies. The UV-vis data (Fig. 3) reveal that photon harvesting scales primarily with the surface area (and by extension dye loading). Even though more rutile in mixed-phase $TiO_2$ nanocomposites typically resulted in higher photon harvesting, the solar cell measurements revealed that more rutile and photon harvesting did not necessarily lead to higher photocurrents (or efficiencies). It was observed that the photocurrent and efficiency reached the maximum at a rutile content ~13 wt%, while photon harvesting increased all the way to 100 wt% rutile. All the samples tested showed a significant decrease in THz transmission after excitation by a 400 nm pump pulse except R100 (Fig. 5). Note that R100 has a respectable photocurrent of 2 mA cm$^{-2}$. Therefore, the negligible change in THz transmission for the sensitized R100 film cannot be interpreted as revealing the absence of free carriers but merely that they have low mobility. Electron transport within the synthesized rutile nanorods likely involved electrons hopping between surface defects or other trapping sites. As discussed previously, the synthesized rutile nanorods have a relatively low degree of crystallinity (Fig. 1f) and consequently abundant surface defects as electron trapping sites. In THz studies, injected electrons initially bound at surface sites are invisible or less visible to the THz probe.[49,50]

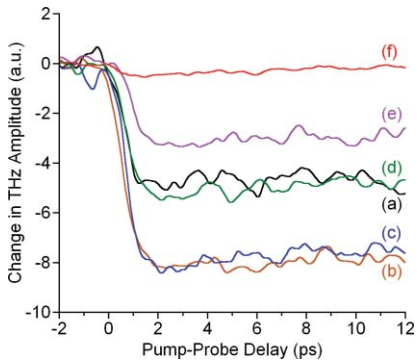


**Fig. 5** 400 nm pump/THz probe of electron injection in N719-sensitized $TiO_2$ films: (a) R0, (b) R5, (c) R13, (d) R19, (e) R40, and (f) R100.

As the amount of rutile in the mixed-phase $TiO_2$ decreased, the THz absorption increased until the nanocomposite with 13 wt% rutile, at which point THz absorption decreased again. Considering the UV-vis, solar cell, and THz data together, we see that the sensitized rutile (R100) harvests photons most efficiently but nonetheless delivers less than half the number of electrons (under short-circuit conditions) than more weakly absorbing R13 having only ~13 wt% rutile. The THz results suggest that the significantly lower photocurrent in the mixed-phase nanocomposites with relatively high rutile content can be ascribed to low electron mobility due to the relatively low degree of crystallinity of the synthesized rutile nanorods. In fact, Fig. 5f suggests that electron transport in the synthesized rutile $TiO_2$ was so slow as to be virtually invisible to the THz probe. The fact that both THz absorption and solar efficiency have their maxima at the same rutile percentage (between 10 wt% and 15 wt%) suggests that at least some electrons migrate from the more efficient light-harvester, rutile, to the anatase conduction band where electrons are more mobile. If an electron flux from rutile to anatase did not occur, the THz absorption would have continued increasing together with the anatase concentration up to R0. In contrast, THz spectroscopy confirmed that the highest mobile electron current occurs within anatase at exactly the same phase composition that has the highest macroscopic photocurrents and efficiencies.

The conduction band electrons in the sensitized R100 film have a much shorter lifetime than in other $TiO_2$ materials (see Fig. S1 in ESI).† One may argue that interfacial recombination between the injected electrons and the oxidized N719 dye molecules could explain both the small change in THz transmission and the short lifetime of conduction band electrons for the sensitized R100 (rutile) sample. This is very unlikely since the open-circuit voltage for the R100 cell would be much lower than the observed value (0.76 V, see Table 1) if significant interfacial charge recombination occurs. The rutile nanorods can absorb a small portion of visible light (< 415 nm) due to its relatively smaller band gap (3.0 *vs.* 3.2 eV for anatase phase).[27] The 400 nm pump pulse used in THz studies can initiate both the photoexcitation of surface N719 dye molecules and the band gap excitation of rutile nanorods. Therefore, the short lifetime of a fraction of the conduction band electrons in R100 can be explained by the recombination of photo-excited electron–hole pairs in the rutile nanorods.

### Effect of $TiCl_4$ treatment

The fabrication of high efficiency DSSCs usually involves treating $TiO_2$ thin films with a dilute solution of $TiCl_4$ prior to dye sensitization.[46] In this study, different $TiO_2$ photoanodes were also treated with a dilute solution of $TiCl_4$ at room temperature. Significant improvement in the photocurrent was observed for all of the samples (Table 1). Consequently, the overall solar conversion efficiencies increased by 0.95% for the P25 cell and by 0.54–0.63% for other cells. At the same time, the $TiCl_4$ treatment slightly lowers photovoltage due to an increased population of surface trapping sites.[51]

The $TiCl_4$ treatment generally improves the photocurrent and efficiency of $TiO_2$ thin films for a variety of reasons. For example, the $TiCl_4$ treatment can enhance the roughness, surface area, and dye adsorption of $TiO_2$ thin films.[46,51] Other possible reasons include the formation of new layers of rutile upon the $TiCl_4$ treatment, enhancing the interparticle connection and electron transport properties of $TiO_2$ thin films.[23,52,53] Different opinions exist regarding the effect of the $TiCl_4$ treatment. Sommeling and co-workers demonstrated that the improved efficiency was not a consequence of a higher dye loading or better charge transport after the $TiCl_4$ treatment.[54] Instead, the researchers suggested that the enhanced charge injection and photocurrent was due to a downward shift in the $TiO_2$ conduction band edge and a decrease in the interception rate of injected electrons by the electrolyte.[54,55]

This present study looks at the effect of rutile content in the photovoltage–current performance of mixed-phase $TiO_2$ photoanodes. Because the $TiCl_4$ treatment of $TiO_2$ films usually leads to the formation of rutile nanocrystals,[23] this study can be considered as potentially applicable to the role of the $TiCl_4$ treatment in DSSCs. The photovoltaic performance of different DSSCs as a function of rutile content is summarized in Fig. 6. A strong correlation can be found between the change in THz transmission of N719-sensitized $TiO_2$ films and the photovoltaic performance of corresponding DSSCs.

### The synergistic effect between anatase and rutile in DSSCs

As mentioned earlier, the decrease in THz transmission amplitude can be considered a measure of the amount of electrons in the anatase conduction band injected from the photo-excited N719 dye molecules or transferred from the rutile phase. Therefore, the addition of rutile nanorods at relatively low rutile content resulted in more conduction band electrons in anatase and higher efficiencies of the R5 and R13 cells. This confirms that electron transfer can occur from rutile to anatase in DSSCs. It might appear that such electron migration would be thermodynamically prohibited because the conduction band of pure-phase anatase is typically 0.2 eV more negative than that of rutile.[22] In heterogeneous photocatalysis, the synergistic effect between anatase and rutile was indeed explained by the interfacial electron migration from the rutile conduction band to anatase trapping sites.[27] Such electron migration is energetically allowed because the anatase trapping sites lie below the rutile conduction band.[56]

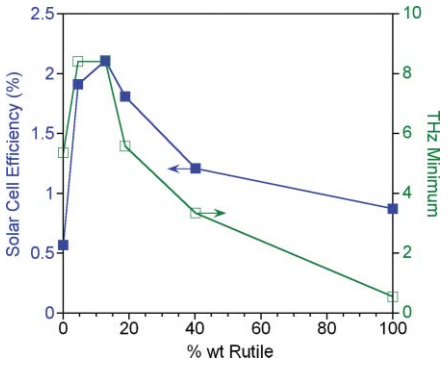


**Fig. 6** DSSC efficiencies (solid squares) and THz transmission minima (open squares) of corresponding N719-sensitized $TiO_2$ films as a function of rutile weight percentage.

In this study, the rutile nanorods have a greater surface area and a much higher dye loading than the anatase NPs (Fig. 3). Upon photoexcitation, different numbers of electrons were injected from the surface coordinated dye molecules to $TiO_2$ NPs. The accumulation of electrons on $TiO_2$ NPs could change the relative position of conduction band edges at the anatase-rutile grain boundary, allowing the electron migration from the rutile nanorods to the anatase NPs. In this proposed model, electrons generated in dye-sensitized rutile nanorods migrate to the anatase NPs before being collected and passing through the external load. At relatively low rutile content, such electron migration enhanced the photocurrent and led to the observed synergistic effect between anatase and rutile.

We suggest that, even if the rutile conduction band edge remained ~0.2 eV negative of the anatase conduction band edge in mixed-phase nanocomposites, the proposed electron transfer would still be possible, even perhaps likely. If we use a Boltzmann distribution to describe the energy distribution of electrons in the rutile conduction band, 0.05% of the electrons would have enough energy to clear a 0.2 eV barrier at room temperature. This does not even take into account that electrons injected into the rutile nanorods are probably 'hot' because the energy of the dye excited state is significantly higher than the rutile conduction band. In line with this proposal, the THz results suggest that electron transfer from rutile to anatase in the mixed-phase $TiO_2$ probably occurs within the first picosecond after photoexcitation and electron injection is thus faster than the typical equilibration times with the

 

lattice. Furthermore, the much higher mobility and lower spatial confinement of free electrons in anatase would result in very few electrons "returning" to rutile once they have been transferred to anatase.

Another model is thermodynamic. As electrons are efficiently injected but confined within the rutile nanorods, both by the physical size and the low mobility of the rutile, the Fermi level within the rutile nanorods will rise (as compared to where it would be without illumination). On the other hand, electrons within anatase are efficiently removed by their higher mobility and, hence, the Fermi level of anatase remains closer to its dark equilibrium with rutile. Therefore, a thermodynamic dis-equilibrium will occur that will drive electron transfer from rutile to anatase. The Fermi energy/Gibbs free energy gradient thus established contains both a concentration component (electron build-up in rutile relative to anatase) and an entropy component (less confinement in anatase). This thermodynamic picture, supported by the experimental data, suggests that an electron flux will be established from rutile to anatase within a working DSSC under steady state conditions.

Finally, there is a morphological factor that may contribute to the detrimental effect of relatively high rutile content in the DSSC performance. In this study, the anatase and rutile NPs are spherical and rod-like, respectively. At high rutile content, the surfaces of anatase NPs are saturated with rutile nanorods; further addition of rutile may trigger accelerated interception of injected electrons by the electrolyte, resulting in decreased photocurrent and photovoltage (R40, Table 1).

## Conclusions

Wide bandgap semiconductors such as $TiO_2$ have been widely employed as heterogeneous photocatalysts for environmental and energy applications. In DSSCs, mesoscopic $TiO_2$ films are used to collect photo-excited electrons from light-harvesting dye molecules. The anatase phase of $TiO_2$ is usually the preferred polymorph as heterogeneous photocatalysts and the electron acceptors in DSSCs. A synergistic effect exists between anatase and rutile NPs, in which interfacial electron transfer occurs from the rutile NPs to the anatase NPs.

In this study, we prepared DSSCs using $TiO_2$ photoanodes that differ only in phase composition. The addition of rutile significantly enhanced the photocurrent and overall solar conversion efficiency of anatase photoanodes. An optimal rutile content around 13 wt% is found; at higher percentages, the addition of rutile appears to be detrimental to the DSSCs. Time-resolved THz spectroscopy was employed to investigate the underlying mechanism for the synergistic effect in DSSCs by studying the charge injection of dye-sensitized mixed-phase $TiO_2$ thin films. Our THz results clearly demonstrate that photoexcited electrons injected into rutile NPs can transfer to the conduction band of anatase NPs. Based on a correlation between the photovoltaic and THz results, electron migration from rutile to anatase is considered to explain the enhanced photovoltaic performance of mixed-phase $TiO_2$ solar cells and the beneficial effect of $TiCl_4$ treatment as reported in the literature. The synergistic effect can be utilized to fabricate DSSCs with improved efficiencies using mixed-phase $TiO_2$ photoanodes.

## Experimental

### Materials synthesis and characterization

The commercially available P25 $TiO_2$ was used as received from Degussa (now Evonik). Mixed-phase $TiO_2$ nanocomposites were prepared from commercial anatase powder (Sigma–Aldrich, 99.8%) and rutile nanorods synthesized *via* a low-temperature hydrothermal method.[44] Prior to the hydrothermal process, 20 mL of titanium(IV) chloride (Sigma–Aldrich, 99.9%) were hydrolyzed in 200 mL of Milli-Q water, forming a light milky solution after stirring at room temperature for 90 min. The solution was then mixed with 5 mL of 5 v/v% Triton X-100 (Baker) in ethanol and was refluxed at 373 K for 18 h. Subsequent characterization with XRD and SEM confirmed the formation of rod-like, pure-phase rutile. The rutile nanorods were then mixed with a certain amount of commercial anatase and were stirred at room temperature for 12 h. Finally, the mixtures were centrifuged and washed with water until a pH $>$ 5 was obtained. Pure rutile nanorods were also collected following the same procedure and without adding anatase.

Thin films (dimension 0.5 cm $\times$ 1 cm, thickness ~10 μm) of $TiO_2$ NPs were prepared by a doctor-blade method on FTO glasses (Tec 8, light transmittance 77%, Hartford Inc., USA). Photoanodes for use in DSSCs were obtained by drying the thin films on FTO glasses at room temperature and sintering at 450 °C for 2 h (ramp rate 5 °C $min^{-1}$). For SEM studies, the photoanodes were coated with Au and were examined with a field-emission scanning electron microscope (FEI XL30 ESEM-FEG).

A set of photoanodes were also treated with a solution of $TiCl_4$. Prior to the $TiCl_4$ treatment, 1 mL of titanium(IV) chloride (Sigma–Aldrich, 99.9%) was hydrolyzed in 100 mL of Milli-Q water at 0 °C, forming a clear solution after stirring at 0 °C for 90 min. Photoanodes were soaked in the $TiCl_4$ solution at room temperature for 12 h and washed thoroughly with Milli-Q water. The photoanodes were then dried at room temperature and were sintered at 450 °C for 2 h for use in DSSCs.

The XRD patterns of pure- and mixed-phase $TiO_2$ samples after thermal treatment at 450 °C were recorded on a Bruker-AXS D8 Focus diffractometer ($\lambda = 1.5418$ Å, CuKα radiation, step time 1 s, step size 0.05°) over the range of $20° < 2\theta < 60°$.[47] Specific surface areas of the same $TiO_2$ materials in powder form were measured with a Quantachrome Autosorb-3b static volumetric instrument.

For the UV-vis studies, thin films of different $TiO_2$ samples were prepared by the doctor-blade method on microscopic slides and subject to thermal treatment at 450 °C. The thin films were then sensitized with N719 dye by soaking in an ethanol solution of 0.22 mM N719 overnight and dried at room temperature before collecting UV-visible spectra with a Varian Cary 3 spectrophotometer in diffuse reflectance geometry.[57] The same sensitized films were also used in THz studies.

### Fabrication and testing of DSSC devices

The photoanodes, after sintering at 450 °C, were sensitized with N719 by soaking in an ethanol solution of 0.22 mM N719 overnight. Counter electrodes were prepared by coating with two drops of 0.05 M hexachloroplatinic acid in ethanol on a FTO plate and heating at 400 °C for 15 min. An electrolyte solution was prepared containing 0.6 M *tert*-butyl ammonium iodide,

0.04 M iodine, 0.025 M lithium iodide, 0.05 M guanidinium thiocyanate, and 0.28 M *tert*-butyl pyridine in a 15 : 85 (v/v) mixture of valeronitrile and acetonitrile.[58] To assemble a DSSC, a dye-sensitized photoanode and a counter electrode were sealed to a sandwich-type cell by heating with 120 μm thick thermoplast hot-melt sealing foil (SX1170-60, SOLARONIX SA, Switzerland) as a spacer between the electrodes. The electrolyte solution was injected into the cell from the counter electrode side through two pre-drilled holes, and then the holes were sealed with the thermoplast hot-melt sealing foil and a piece of Al foil by heating. The DSSC was allowed to stay at room temperature for 3 h before photocurrent–voltage ($I$–$V$) measurement.

The irradiation source for the $I$–$V$ measurement is a 300 W ozone-free xenon lamp equipped with a 50% IR blocking filter (Newport, USA), which simulates solar light. The light intensity was calibrated to be 100 mW $cm^{-1}$.[2] The current–voltage curves were obtained by measuring the photocurrent of the cells using a Keithley model 2400 digital source meter (Keithley, USA) under an applied external potential scan.

### Terahertz studies

In THz studies, an amplified Ti:Sapphire laser (Tsunami/Spitfire from Spectra Physics) generated 800 mW of pulsed near-IR light at a 1 kHz repetition rate. The pulse width was ~100 fs, and the center wavelength was 800 nm. Roughly two-thirds of the power was frequency doubled and then filtered to produce 50 mW of 400 nm (3.11 eV) light for the pump beam. The remainder of the near-IR light was used to generate and detect THz radiation using a 4-paraboloid arrangement that focused the THz beam to a spot size of ~3 mm at the sample. Terahertz radiation was generated using optical rectification in a ZnTe(110) crystal and detected using free space electrooptic sampling in a second ZnTe(110) crystal. Terahertz data were taken at room temperature with the sample moving to avoid photobleaching. The average of three samples was taken for each data set. Further information on the spectrometer and techniques was reported in the literature.[48,49]

Terahertz radiation was absorbed by mobile electrons in the $TiO_2$ conduction band and was insensitive to electrons within the absorbed sensitizer. A decrease in broadband THz (0.2–2 THz) transmission in photo-excited samples compared to non-photo-excited samples indicated a higher electron density in the $TiO_2$. Injection time measured by monitoring the change in THz transmission as the delay time between the 400 nm pump and the THz probe was varied.

## Acknowledgements

The authors acknowledge support from the Chemical Sciences, Geosciences, and Biosciences Division, Office of Basic Energy Sciences, Office of Science, U. S. Department of Energy (DE-FG02-07ER15909). The generous donation of P25 $TiO_2$ by Evonik is greatly appreciated. G. L. thanks Daryl Smith, Xiaoming Wang, Prof. Gary Haller, Dr Christopher Incarvito, and Dr Zhenting Jiang for their kind assistance in various aspects of the experiments.

## References

1 B. O'Regan and M. Grätzel, *Nature*, 1991, **353**, 737–740.
2 M. Grätzel, *Nature*, 2001, **414**, 338–344.
3 M. Grätzel, *Inorg. Chem.*, 2005, **44**, 6841–6851.
4 L. M. Peter, *J. Phys. Chem. C*, 2007, **111**, 6601–6612.
5 L. M. Peter, *Phys. Chem. Chem. Phys.*, 2007, **9**, 2630–2642.
6 T. W. Hamann, R. A. Jensen, A. B. F. Martinson, H. Van Ryswyk and J. T. Hupp, *Energy Environ. Sci.*, 2008, **1**, 66–78.
7 G. J. Meyer, *Inorg. Chem.*, 2005, **44**, 6852–6864.
8 D. F. Watson and G. J. Meyer, *Annu. Rev. Phys. Chem.*, 2005, **56**, 119–156.
9 J. R. Durrant, S. A. Haque and E. Palomares, *Coord. Chem. Rev.*, 2004, **248**, 1247–1257.
10 M. K. Nazeeruddin, F. De Angelis, S. Fantacci, A. Selloni, G. Viscardi, P. Liska, S. Ito, B. Takeru and M. Grätzel, *J. Am. Chem. Soc.*, 2005, **127**, 16835–16847.
11 B. C. O'Regan, K. Walley, M. Juozapavicius, A. Anderson, F. Matar, T. Ghaddar, S. M. Zakeeruddin, C. Klein and J. R. Durrant, *J. Am. Chem. Soc.*, 2009, **131**, 3541–3548.
12 F. Gao, Y. Wang, D. Shi, J. Zhang, M. Wang, X. Jing, R. Humphry-Baker, P. Wang, S. M. Zakeeruddin and M. Grätzel, *J. Am. Chem. Soc.*, 2008, **130**, 10720–10728.
13 D. Kuang, S. Ito, B. Wenger, C. Klein, J. E. Moser, R. Humphry-Baker, S. M. Zakeeruddin and M. Grätzel, *J. Am. Chem. Soc.*, 2006, **128**, 4146–4154.
14 A. B. F. Martinson, T. W. Hamann, M. J. Pellin and J. T. Hupp, *Chem.–Eur. J.*, 2008, **14**, 4458–4467.
15 K. Shankar, J. I. Basham, N. K. Allam, O. Varghese, G. K. Mor, X. Feng, M. Paulose, J. A. Seabold, K.-S. Choi and C. A. Grimes, *J. Phys. Chem. C*, 2009, **113**, 6327–6359.
16 G. K. Mor, O. K. Varghese, M. Paulose, K. Shankar and C. A. Grimes, *Sol. Energy Mater. Sol. Cells*, 2006, **90**, 2011–2075.
17 M. Zukalova, A. Zukal, L. Kavan, M. K. Nazeeruddin, P. Liska and M. Grätzel, *Nano Lett.*, 2005, **5**, 1789–1792.
18 J. Wu, S. Hao, J. Lin, M. Huang, Y. Huang, Z. Lan and P. Li, *Cryst. Growth Des.*, 2008, **8**, 247–252.
19 Y. Lu, D.-J. Choi, J. Nelson, O. B. Yang and B. A. Parkinson, *J. Electrochem. Soc.*, 2006, **153**, E131–E137.
20 A. Fillinger, D. Soltz and B. A. Parkinson, *J. Electrochem. Soc.*, 2002, **149**, A1146–A1156.
21 D. Cahen, G. Hodes, M. Grätzel, J. F. Guillemoles and I. Riess, *J. Phys. Chem. B*, 2000, **104**, 2053–2059.
22 L. Kavan, M. Grätzel, S. E. Gilbert, C. Klemenz and H. J. Scheel, *J. Am. Chem. Soc.*, 1996, **118**, 6716–6723.
23 S. Kambe, S. Nakade, Y. Wada, T. Kitamura and S. Yanagida, *J. Mater. Chem.*, 2002, **12**, 723–728.
24 N. G. Park, J. van de Lagemaat and A. J. Frank, *J. Phys. Chem. B*, 2000, **104**, 8989–8994.
25 D. C. Hurum, A. G. Agrios, S. E. Crist, K. A. Gray, T. Rajh and M. C. Thurnauer, *J. Electron Spectrosc. Relat. Phenom.*, 2006, **150**, 155–163.
26 G. Li and K. A. Gray, *Chem. Phys.*, 2007, **339**, 173–187.
27 D. C. Hurum, A. G. Agrios, K. A. Gray, T. Rajh and M. C. Thurnauer, *J. Phys. Chem. B*, 2003, **107**, 4545–4549.
28 D. C. Hurum, K. A. Gray, T. Rajh and M. C. Thurnauer, *J. Phys. Chem. B*, 2005, **109**, 977–980.
29 R. I. Bickley, T. Gonzalezcarreno, J. S. Lees, L. Palmisano and R. J. D. Tilley, *J. Solid State Chem.*, 1991, **92**, 178–190.
30 T. Ohno, K. Tokieda, S. Higashida and M. Matsumura, *Appl. Catal., A*, 2003, **244**, 383–391.
31 D. Jiang, S. Zhang and H. Zhao, *Environ. Sci. Technol.*, 2007, **41**, 303–308.
32 L. Chen, M. E. Graham, G. Li and K. A. Gray, *Thin Solid Films*, 2006, **515**, 1176–1181.
33 G. Li, S. Ciston, Z. Saponjic, L. Chen, N. Dimitrijevic, T. Rajh and K. A. Gray, *J. Catal.*, 2008, **253**, 105–110.
34 G. Li, L. Chen, M. E. Graham and K. A. Gray, *J. Mol. Catal. A: Chem.*, 2007, **275**, 30–35.
35 B. Sun and P. G. Smirniotis, *Catal. Today*, 2003, **88**, 49–59.
36 A. Mills and S. LeHunte, *J. Photochem. Photobiol., A*, 1997, **108**, 1–35.
37 B. Koo, J. Park, Y. Kim, S.-H. Choi, Y.-E. Sung and T. Hyeon, *J. Phys. Chem. B*, 2006, **110**, 24318–24323.
38 C. S. Karthikeyan, M. Thelakkat and M. Willert-Porada, *Thin Solid Films*, 2006, **511–512**, 187–194.
39 I. Kartini, D. Menzies, D. Blake, J. C. D. da Costa, P. Meredith, J. D. Riches and G. Q. Lu, *J. Mater. Chem.*, 2004, **14**, 2917–2921.
40 T. L. Thompson and J. T. Yates Jr., *Chem. Rev.*, 2006, **106**, 4428–4453.

 

41 S. G. Abuabara, C. W. Cady, J. B. Baxter, C. A. Schmuttenmaer, R. H. Crabtree, G. W. Brudvig and V. S. Batista, *J. Phys. Chem. C*, 2007, **111**, 11982–11990.
42 M. Gopal, W. J. M. Chan and L. C. DeJonghe, *J. Mater. Sci.*, 1997, **32**, 6001–6008.
43 G. Li and K. A. Gray, *Chem. Mater.*, 2007, **19**, 1143–1146.
44 G. Li, N. Dimitrijevic, L. Chen, T. Rajh and K. A. Gray, *J. Phys. Chem. C*, 2008, **112**, 19040–9044.
45 H. Z. Zhang and J. F. Banfield, *J. Phys. Chem. B*, 2000, **104**, 3481–3487.
46 S. Ito, T. N. Murakami, P. Comte, P. Liska, C. Grätzel, M. K. Nazeeruddin and M. Grätzel, *Thin Solid Films*, 2008, **516**, 4613–4619.
47 G. Li, E. M. Sproviero, R. C. Snoeberger, III, N. Iguchi, J. D. Blakemore, R. H. Crabtree, G. W. Brudvig and V. S. Batista, *Energy Environ. Sci.*, 2009, **2**, 230–238.
48 J. B. Baxter and C. A. Schmuttenmaer, *J. Phys. Chem. B*, 2006, **110**, 25229–5239.
49 M. C. Beard, G. M. Turner and C. A. Schmuttenmaer, *Phys. Rev. B: Condens. Matter Mater. Phys.*, 2000, **62**, 15764–5777.
50 G. M. Turner, M. C. Beard and C. A. Schmuttenmaer, *J. Phys. Chem. B*, 2002, **106**, 11716–11719.
51 S. Ito, P. Liska, P. Comte, R. Charvet, P. Pechy, U. Bach, L. Schmidt-Mende, S. M. Zakeeruddin, A. Kay, M. K. Nazeeruddin and M. Grätzel, *Chem. Commun.*, 2005, 4351–4353.
52 M. Y. Song, D. K. Kim, S. M. Jo and D. Y. Kim, *Synth. Met.*, 2005, **155**, 635–638.
53 M. Y. Song, D. K. Kim, K. J. Ihn, S. M. Jo and D. Y. Kim, *Nanotechnology*, 2004, **15**, 1861–1865.
54 P. M. Sommeling, B. C. O'Regan, R. R. Haswell, H. J. P. Smit, N. J. Bakker, J. J. T. Smits, J. M. Kroon and J. A. M. van Roosmalen, *J. Phys. Chem. B*, 2006, **110**, 19191–19197.
55 B. C. O'Regan, J. R. Durrant, P. M. Sommeling and N. J. Bakker, *J. Phys. Chem. C*, 2007, **111**, 14001–14010.
56 S. Leytner and J. T. Hupp, *Chem. Phys. Lett.*, 2000, **330**, 231–236.
57 W. R. McNamara, R. C. Snoeberger, III, G. Li, J. M. Schleicher, C. W. Cady, M. Poyatos, C. A. Schmuttenmaer, R. H. Crabtree, G. W. Brudvig and V. S. Batista, *J. Am. Chem. Soc.*, 2008, **130**, 14329–14338.
58 S. Kim, J. K. Lee, S. O. Kang, J. Ko, J. H. Yum, S. Fantacci, F. D. Angelis, D. D. Censo, M. K. Nazeeruddin and M. Grätzel, *J. Am. Chem. Soc.*, 2006, **128**, 16701–16707.